

LETTER

Open Access



# Vectorial liquid-crystal holography

Ze-Yu Wang<sup>1</sup>, Zhou Zhou<sup>2</sup>, Han Zhang<sup>1</sup>, Yang Wei<sup>1</sup>, Hong-Guan Yu<sup>1</sup>, Wei Hu<sup>1</sup>, Wei Chen<sup>1</sup>, Hai-Tao Dai<sup>3</sup>,  
Ling-Ling Ma<sup>1\*</sup>, Cheng-Wei Qiu<sup>2\*</sup> and Yan-Qing Lu<sup>1\*</sup>

## Abstract

Vectorial optics with fine inhomogeneous polarization control are highly desired. Metasurfaces have been captivated a promising candidate, but their static post-fabrication geometry largely limits the dynamic tunability. Liquid crystal (LC) is usually employed as an additional index-changing layer together with metasurfaces. Unfortunately, most of the reported LCs only impart a varying but uniform phase on top of that from the metasurface, which we term “scalar” LC optics. Here, we pixelate a single-layer LC to display versatile and tunable vectorial holography, in which the polarization and amplitude could be arbitrarily and independently controlled at varying spatial positions. Furthermore, the subtle and vectorial LC-holography highlights the broadband and electrically-switchable functionalities. Our vectorial LC holography reveals significant opportunities for advanced cryptography, super-resolution imaging, and many other applications.

**Keywords** Liquid crystals, Vectorial optics, Holography

## 1 Introduction

As a technique for optical waveform control, holography has emerged as a powerful tool for various applications from augmented reality and virtual reality to data storage and optical encryption [1–6]. It allows for a complete reconstruction of the wavefront of light [7–11]. To explore the full potential of multichannel optical communications and enhanced optical encryption, many efforts have been made in vectorial holography [12–17], which involves the manipulation of both polarization and

amplitude in a spatially varying fashion. Among different methods, metasurfaces, consisting of subwavelength structure units, have been proven to be highly effective in engineering the waveform of electromagnetic waves with an unprecedented level of precision [18–21]. By virtue of the multiple design freedom, vectorial meta-holograms with arbitrary polarization control spring up using diatomic plasmonic metasurfaces, geometric phase dielectric metasurfaces, or gallium nitride based pixelated metasurfaces [22–26]. However, the static geometry of lithography-based metasurfaces inevitably limits the dynamic and continuous tunability in holography. For versatile applications, smart responsive vectorial optical platforms together with easy fabrication and enhanced functionality are highly demanded.

Liquid crystal (LC), a self-organized soft material that intrinsically shares the anisotropic property of crystals and the fluidity of liquids, has already become a dominant force in the display market and also a rising star in various non-display fields [27–31]. Particularly, the geometric phase LCs have drawn extensive attention in optical waveform control with the merits of lithography-free fabrication, flexible tunability, high efficiency, planar configuration, and broad bandwidth,

\*Correspondence:

Ling-Ling Ma  
malingling@nju.edu.cn  
Cheng-Wei Qiu  
chengwei.qiu@nus.edu.sg  
Yan-Qing Lu  
yqlu@nju.edu.cn

<sup>1</sup> National Laboratory of Solid State Microstructures, Key Laboratory of Intelligent Optical Sensing and Manipulation, Collaborative Innovation Center of Advanced Microstructures, College of Engineering and Applied Sciences, Nanjing University, Nanjing 210023, China

<sup>2</sup> Department of Electrical and Computer Engineering, National University of Singapore, Singapore 117583, Singapore

<sup>3</sup> Tianjin Key Laboratory of Low Dimensional Materials Physics and Preparing Technology, School of Science, Tianjin University, Tianjin 300072, China

resulting in promising applications, including spatial light modulation, information storage, holographic imaging, etc. [32–34]. However, as a phase-only material (modifies the phase of light only in the near-field), LC single-material vectorial holography has been captivated impossible and never been explored before. Conventional LC devices can only implement scalar optical holography, where the LC-hologram is limited

to control the intensity distribution of the holographic images with uniform polarization and random phase profiles [35–37] (Fig. 1a). Recent efforts have also been made by integrating LCs with metasurfaces to incorporate the tunability [38–41]. Unfortunately, the fabrication becomes further cumbersome, and most of the reported LCs can only impart a varying but uniform phase retardation on top of that from the metasurfaces.

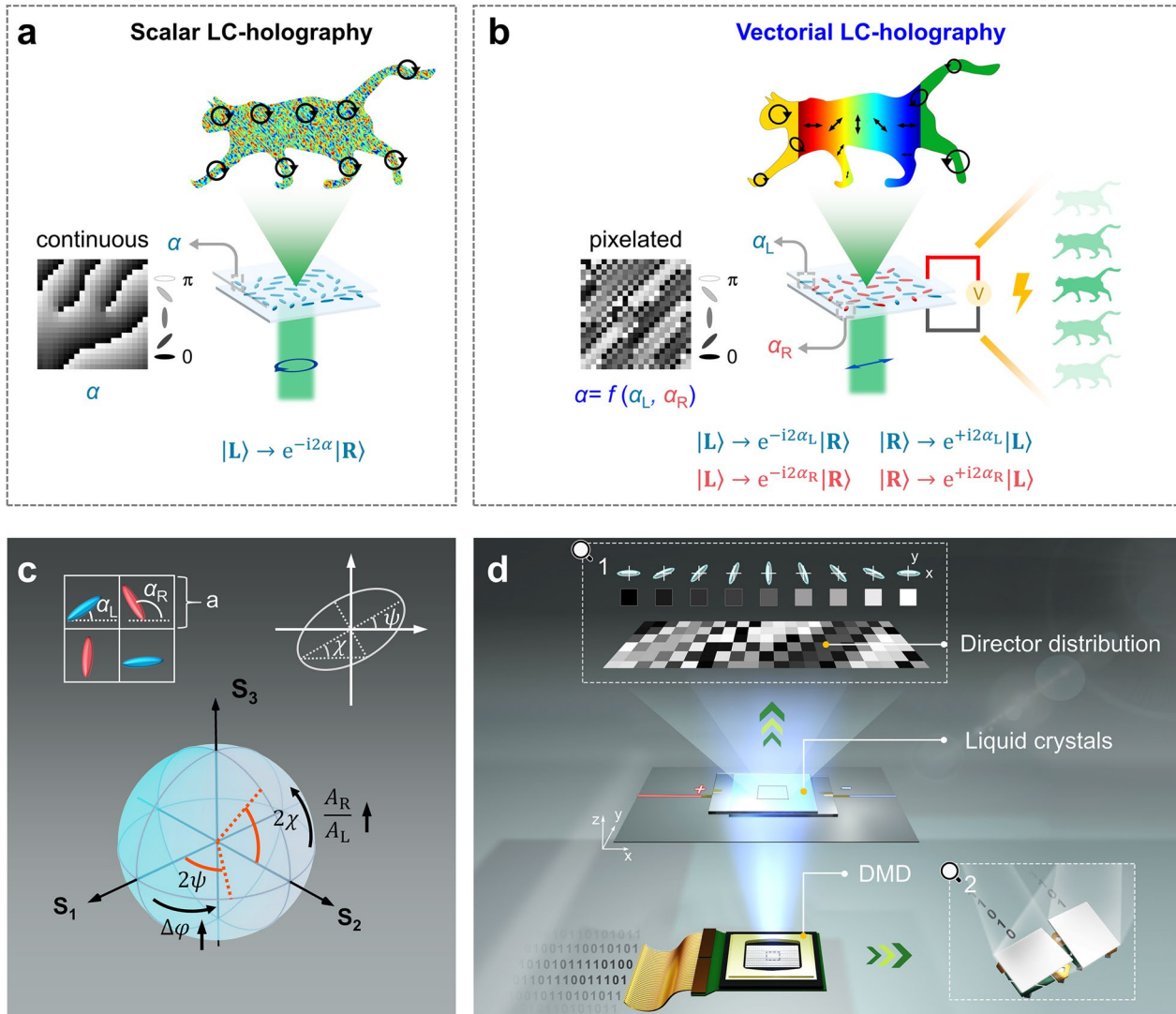


**Fig. 1** Schematic illustrations of scalar and vectorial LC-holography. **a** Scalar LC-holography. Holographic image (a cat) is reconstructed with a random phase distribution ( $\varphi_R$ ) when illuminated by LCP light. **b** Vectorial LC-holography. We spatially multiplexing the LC holograms for LCP and RCP into a single LC layer, which are indicated by blue and red LC directors. Two independent holographic images (a cat without a tail and a cat without a head) are generated with spatially variant amplitudes and phase differences when illuminated by linearly polarized light. These two images are partially overlapped. The vectorial pattern is determined by both the phase difference distribution ( $\Delta\varphi$ ) and amplitude ratio ( $A_R/A_L$ ).  $a$  is the azimuthal angle distribution of LC directors. **c** Poincaré sphere together with the polarization ellipse to denote the polarization state by the azimuth angle  $\psi$  and the ellipticity angle  $\chi$ . A nested LC director field with four blue and red LC pixels are depicted. The LC directors within each LC domain are uniformly aligned.  $a$  denotes the size of each LC pixel. **d** Photopatterning of single-material LC superstructures for vectorial LC holography. The insets in dashed boxes 1 and 2 are larger versions of the LC director distribution represented by a pixelated grey-scale pattern and typical digital micro-mirrors in the digital micro-mirror device (DMD) based micro-lithography system, respectively

Single-material vectorial LC-holography with arbitrary space-variant polarization and intensity control is still challenging.

To tackle this dilemma, we demonstrate a novel single-material LC encoding method to display versatile and tunable vectorial holography, in which both the polarization and amplitude are arbitrarily controlled at varying positions (Fig. 1b). With a proposed two-loop-iteration modified Gerchberg–Saxton (GS) algorithm, we generate helicity multiplexed LC-holograms to synthesize full-vectorial optical fields with unbounded possibilities. The intensity distribution of holographic light field can be selectively and continuously addressed according to the space-variant polarization pattern, which is determined by a weighted superposition of the holographic images for left circular polarization (LCP) and right circular polarization (RCP). By leveraging the dynamic tunability of LCs, we achieve dynamic multichannel vectorial encryption and active vectorial LC-holographic video with the merits of electrical tunability, high efficiency, and broad bandwidth. This work marks the first-ever prototype of lithography-free single-layer LC vectorial holography, which paves a wide and flat avenue to real-world impacts for advanced display, information encryption, and metasurface applications.

## 2 Results

### 2.1 Design strategy for vectorial LC-holography

The design principle for the single-layer and single-material LC vectorial holography is shown in Fig. 1b, c. The LC superstructure consists of a checkerboard distribution of LC directors with helicity multiplexed phase holograms for LCP and RCP. Notably, the LC directors of different colours (blue and red) are the same material but function for different helicities. The transmission matrix of each LC domain can be expressed using the Jones matrix of  $T = R(\alpha) \begin{bmatrix} e^{-i\frac{\Gamma}{2}} & 0 \\ 0 & e^{i\frac{\Gamma}{2}} \end{bmatrix} R(-\alpha)$ , where  $\alpha$  denotes the in-plane orientation angle of the LC director,  $R(\alpha)$  represents the rotation matrix, and  $\Gamma$  is the phase retardation between an ordinary wave and an extraordinary wave. It converts the incident CP light into the opposite helicity with imprinted geometric phases  $e^{\pm i2\alpha}$  ( $|\mathbf{R}\rangle \rightarrow e^{+i2\alpha}|\mathbf{L}\rangle$  and  $|\mathbf{L}\rangle \rightarrow e^{-i2\alpha}|\mathbf{R}\rangle$ , where  $|\mathbf{L}\rangle$  and  $|\mathbf{R}\rangle$  stand for the spin of light). The acquired geometric phases show a linear relation of twice of  $\alpha$ . The conversion efficiency depends on the waveplate transformation implemented by the LC [42].

Considering the incident light with linear polarization (LP) can be decomposed into LCP and RCP, the LP light can be expressed as  $\mathbf{LP}(\theta_{\text{in}}) = e^{i\varphi_{\text{in}}^{\text{L}}}|\mathbf{L}\rangle + e^{i\varphi_{\text{in}}^{\text{R}}}|\mathbf{R}\rangle = e^{i\varphi_{\text{in}}^{\text{R}}}(e^{i\Delta\varphi_{\text{in}}}|\mathbf{L}\rangle + |\mathbf{R}\rangle)$ ,

where  $|\mathbf{L}\rangle = \frac{\sqrt{2}}{2}[1 \quad -i]^{\text{T}}$ ,  $|\mathbf{R}\rangle = \frac{\sqrt{2}}{2}[1 \quad i]^{\text{T}}$ ,  $\varphi_{\text{in}}^{\text{L}}$  ( $\varphi_{\text{in}}^{\text{R}}$ ) represents the phase of the incident light with LCP (RCP), and  $\Delta\varphi_{\text{in}} = \varphi_{\text{in}}^{\text{L}} - \varphi_{\text{in}}^{\text{R}} = 2\theta_{\text{in}}$  ( $\theta_{\text{in}}$  denotes the polarization angle). The generated holographic field  $\mathbf{E}$  in the far-field can be analytically calculated as:

$$\begin{aligned} \mathbf{E} &= A_{\text{R}}e^{i(\varphi_{\text{H}}^{\text{R}}+\varphi_{\text{in}}^{\text{L}})}|\mathbf{R}\rangle + A_{\text{L}}e^{i(\varphi_{\text{H}}^{\text{L}}+\varphi_{\text{in}}^{\text{R}})}|\mathbf{L}\rangle \\ &= e^{i\varphi_{\text{R}}}(A_{\text{R}}|\mathbf{R}\rangle + e^{i\Delta\varphi}A_{\text{L}}|\mathbf{L}\rangle). \end{aligned} \quad (1)$$

Here  $A_{\text{R}}$  ( $A_{\text{L}}$ ) denotes the far-field amplitude distribution of the holographic image of RCP (LCP),  $\varphi_{\text{H}}^{\text{R}}$  and  $\varphi_{\text{H}}^{\text{L}}$  are the designed phase distributions of RCP and LCP,  $e^{i\varphi_{\text{R}}} = e^{i(\varphi_{\text{H}}^{\text{R}}+\varphi_{\text{in}}^{\text{L}})}$ , and  $\Delta\varphi = \varphi_{\text{L}} - \varphi_{\text{R}}$ . In the process of holographic optimization,  $A_{\text{R}}$ ,  $A_{\text{L}}$ , and  $\Delta\varphi$  can be engineered independently and simultaneously, thus allowing for generating an arbitrary state of polarization in the far field. The azimuth angle  $\psi = \frac{1}{2}\Delta\varphi$  and ellipticity angle  $\chi = \frac{1}{2}\arcsin\left(\frac{A_{\text{R}}/A_{\text{L}}-1}{A_{\text{R}}/A_{\text{L}}+1}\right)$  of  $\mathbf{E}$  are depicted in Fig. 1c. The variation in  $\Delta\varphi$  results in a shift of the polarization state along the latitude of Poincaré sphere, and the changes in  $A_{\text{L}}$  and  $A_{\text{R}}$  cause the polarization state to alter along the longitudinal direction. Particularly,  $\Delta\varphi/2$  directly determines the LP distribution in the overlapping area of holographic images of LCP and RCP when  $A_{\text{L}} = A_{\text{R}}$ . For regions with LP state, we can simply use an analyzer to sort the local polarization, and the intensity distribution after the analyzer is calculated as:

$$\begin{aligned} I(\beta) &= |T(\beta) \cdot \mathbf{E}|^2 = \frac{1}{2}A_{\text{R}}^2 + \frac{1}{2}A_{\text{L}}^2 + A_{\text{R}}A_{\text{L}} \\ &\quad \cos(2\beta - \Delta\varphi) = A_{\text{R}}A_{\text{L}}(1 + \cos(2\beta - \Delta\varphi)) \end{aligned} \quad (2)$$

where  $T(\beta)$  is the Jones matrix of an analyzer, and  $\beta$  represents the polarization angle of the analyzer. From Eq. (2), the vectorial information is hidden behind the amplitude of the holographic image, but can be read out by applying an analyzer with a series of specific angles according to the extinction condition (i.e.,  $2\beta - \Delta\varphi = (2N + 1)\pi$ , where  $N$  is an integer).

To independently acquire both the desired intensity and vectorial distribution of holographic images, we propose a two-loop-iteration modified GS algorithm for the single-material vectorial LC-holographic platform. Here, two independent target images are set for LCP and RCP with specific amplitude distributions ( $A_{\text{L}}$  and  $A_{\text{R}}$ ) and a well-defined phase difference distribution ( $\Delta\varphi$ ). As shown in Additional file 1: Fig. S1, our GS algorithm involves two separate iteration loops to optimize the LC phase holograms for LCP and RCP. Meanwhile, we deliberately introduce intermediate steps to establish a correlation between their phase

profiles, allowing for the simultaneous optimization of  $\Delta\varphi$ ,  $A_L$ , and  $A_R$  distributions we have designed (see details in Additional file 1: Text S1). In this case, we manipulate the  $\Delta\varphi$  distribution between holographic images of LCP and RCP while letting their respective phase distributions without intentionally controlled. The local amplitude modulations  $A_L$  and  $A_R$  are assured for producing an on-demand vectorial light field (LCP, RCP, LP, and EP). Consequently, we obtain two phase holograms for LCP and RCP, which are used in the subsequent calculation of the LC director distribution  $\alpha_L$  and  $\alpha_R$ . The final LC director distribution  $\alpha = f(\alpha_L, \alpha_R)$  is obtained by spatially multiplexing  $\alpha_L$  and  $\alpha_R$  together. To minimize crosstalk due to the twin images for LCP and RCP channels, we design the target holographic images in the upper half of the imaging plane.

Different from the scalar LC holography with relatively continuous LC director distribution (Fig. 1a), the helicity multiplexed vectorial LC hologram (Fig. 1b) exhibits a pixelated profile usually with abrupt changes of LC directors within adjacent domains. Such pixelated LC distribution poses challenges to the fabrication. To overcome this issue, the dynamic microlithography photopatterning system are upgraded with high-precision optical components and carefully aligned optical path (Fig. 1d). We achieve the spatial resolution of 1.1  $\mu\text{m}$ , and the precision of the polarization angle is reduced to  $\pm 0.2^\circ$ , allowing for the accurate generation of photoalignment patterns. Then, we proceed to optimize the LC domain size by carrying out a delicate balance between the resolution of the holographic image and the self-assembly quality of pixelated LC superstructures. LC defects and the deviation between the designed and experimental LC directors are avoided as far as possible. More detailed fabrication processes of LC superstructures are provided in Materials and Methods, and Additional file 1: Text S2.

## 2.2 Vectorial LC-holography with programmable polarization control

As a proof of concept, we designed and fabricated three sets of LC superstructures to experimentally demonstrate the vectorial LC holography. We begin by devising a vectorial LC-holographic clock that displays distinct time information based on the polarization keys (analyzer) (Fig. 2a). Two sets of phase holograms are nested ( $\Delta\varphi_L$  for hour hand and  $\Delta\varphi_R$  for minute hand) and encoded into one LC element. The incidence of RCP and LCP light yields independent holographic images of the “hour hand” and “minute hand”, respectively. With LP

light illumination, arbitrary vectorial information can be encoded in areas where the two holographic images overlap. Here, we first consider the case in which the intensity of LCP and RCP holographic images are approximately equal (i.e.,  $A_L \approx A_R$ ). Under this condition, the encoded vectorial information would be LPs at the direction of  $\Delta\varphi/2$ .

For experimental validation, we choose the image in Fig. 2b (displaying the time “15:05:35”) as the target, in which the hour hand and minute hand exhibit circular polarizations, while two numbers of “3” and “5” are encoded with linear polarization directions at  $\pi/4$  and  $-\pi/4$ . The required LC director distribution is then calculated (Additional file 1: Fig. S2), and we simulated the corresponding far-field phase difference ( $\Delta\varphi$ ) between LCP and RCP holographic images (Fig. 2c). As expected, the numbers “3” and “5” can be clearly observed with  $\Delta\varphi$  of  $\pi/2$  and  $-\pi/2$  respectively. With the versatility and high-precision of our photoalignment technique, the designed LC director distribution is pixelated imprinted to the empty LC cell, and a commercial nematic LC E7 is infiltrated and self-assembled into a single-layer LC superstructure. The resulting holographic LC superstructure texture is examined under a crossed polarizing optical microscope (POM), as depicted in Fig. 2d.

Figure 2e presents the observed holographic image at various input/output polarizations (see Additional file 1: Fig. S3 for details of the optical setup). We can see from Fig. 2e(I, II) that helicity multiplexed holographic images of “hour hand” and “minute hand” appear respectively with the incident light of RCP and LCP, providing the time information of 15:05. When the superstructure is illuminated by LP light, the images of “hour hand” and “minute hand” are simultaneously reconstructed, with an overlapping area possessing a uniform “disc” pattern (Fig. 2e(III)). This region carries double-encrypted polarization information corresponding to the encoded phase difference distribution. With polarization keys of  $-45^\circ$  and  $45^\circ$ , we can clearly observe the extinction images of “3” and “5” respectively, thus acquiring the complete time information of 15:05:35 (Fig. 2e(IV, V)). Figure 2e(III) demonstrates the coexistence of polarization states including LCP, RCP, and two states of LP, of which the Stokes parameters ( $S_1$ ,  $S_2$ ,  $S_3$ ) are measured. All the holographic images are of satisfactory quality and highly consistent with our design, implying the potential of our vectorial LC-holography.

## 2.3 Vectorial LC-holography with independent polarization and amplitude control

The continuous control of both the holographic amplitude and vector distributions is further demonstrated. Figure 3a presents the target intensity distribution for the

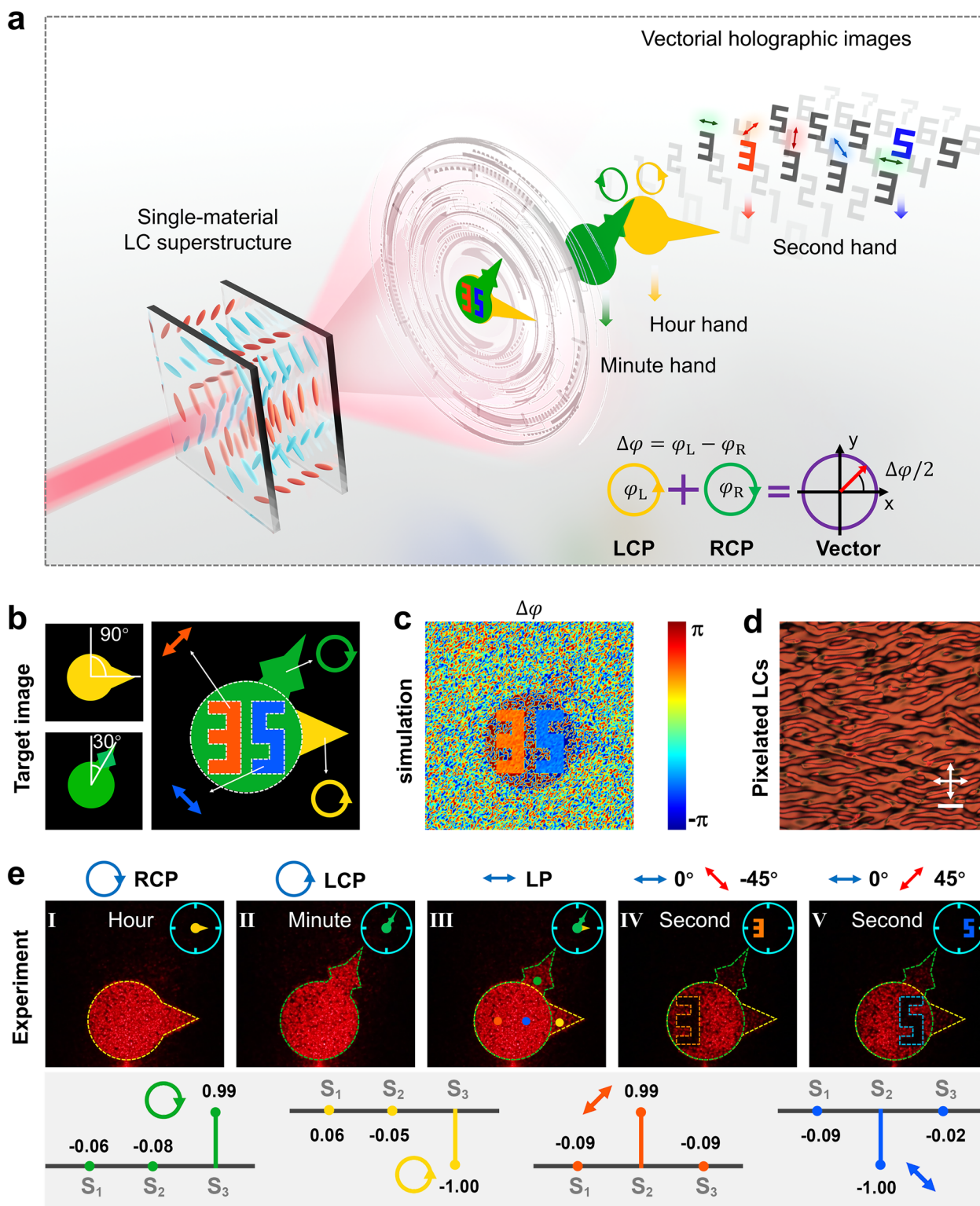


**Fig. 2** Vectorial LC-holographic clock. **a** LC-based vectorial holographic clock for time information encryption. **b** Target holographic images for incident light with RCP, LCP, and LP. The corresponding vectorial information is denoted. **c** Simulated phase difference distribution between the holographic images of LCP and RCP. **d** POM texture of the holographic LC superstructure. The white arrows represent the crossed polarizer and analyzer. Scale bar: 50  $\mu\text{m}$ . **e** Vectorial LC-holographic images at various input/output polarization channels. The blue and red arrows indicate the input and output light polarization, respectively. The measured Stokes parameter values  $S_1, S_2, S_3$  of four typical regions in the LC-holographic clock image (marked by green, yellow, orange, and blue dots) are presented at the bottom

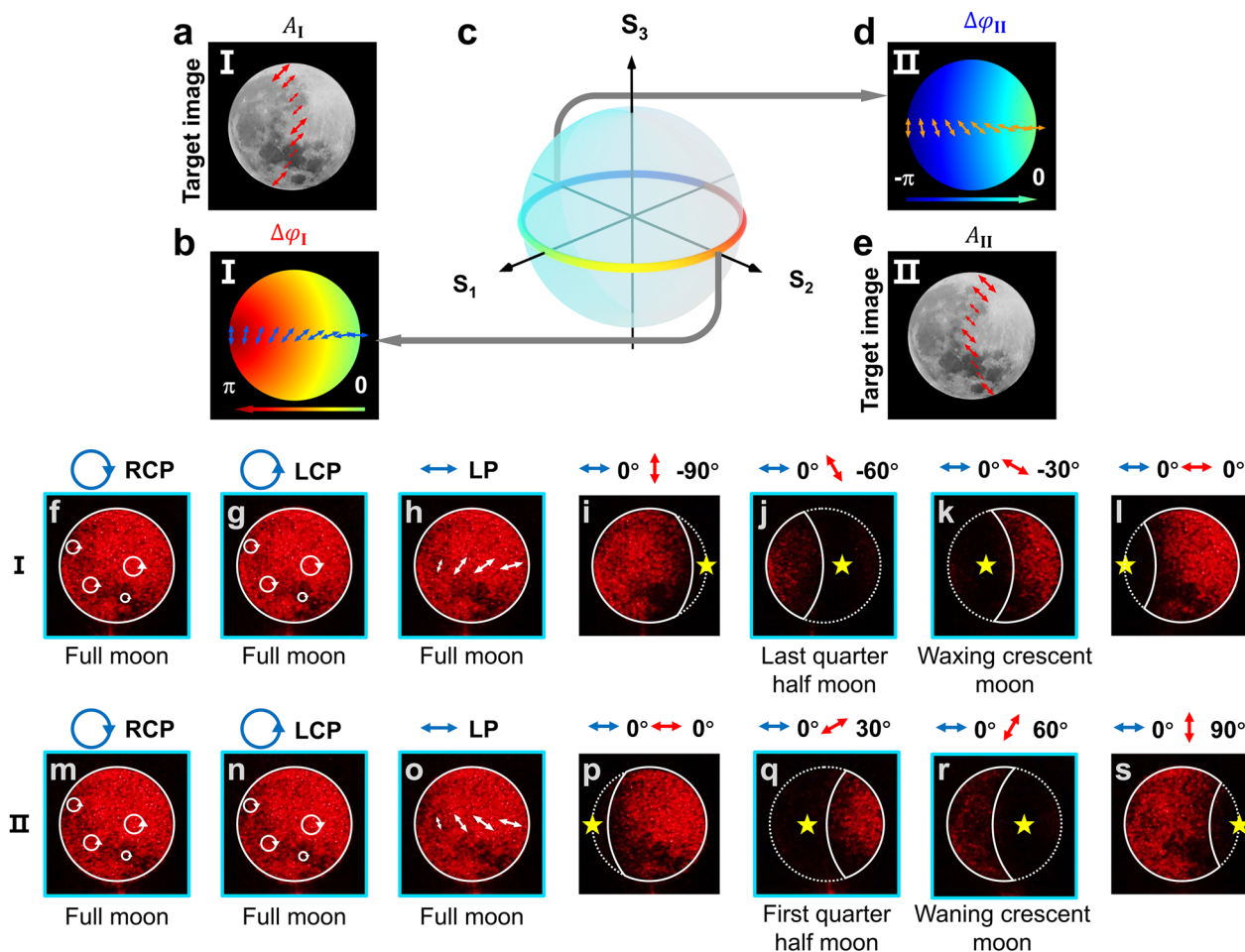


**Fig. 3** Vectorial LC-holographic lunar phases encoded with continuously varied polarization and amplitude distributions. **a–e** Target intensity and phase difference distribution for LC superstructures **(a, b)** I and **(d, e)** II. The double-sided arrows denote typical LP states with different amplitudes at different positions. The continuously varied LPs cover the equator of the Poincaré sphere. **f–s**, Experimental results of vectorial holographic images reconstructed from LC superstructures I and II for incident light with different polarizations. The circles with arrows denote the CP with different helicities and amplitudes. The lengths and directions of arrows indicate the amplitudes and polarizations of LP. The pentagrams represent the darkest position on the holographic image. The holographic images in blue boxes are selected to constitute the full phase diagram of the moon

holographic image I, depicting “the moon” with a continuously varied intensity profile. We continuously encode the phase difference at varying positions (from 0 to  $\pi$ ) to generate the continuous gradient LP profile (Fig. 3b). To align with the lunar phase change, we specially design an arc-shaped phase distribution  $\Delta\varphi_I$ . The arrows in Fig. 3a, b illustrate the distribution of LP, with their directions and lengths indicating the directions and amplitudes of polarization vector field, respectively. For comprehensive vectorial information coverage across the Poincaré sphere’s equator (Fig. 3c), we design another holographic LC superstructure II, which employs the same intensity pattern of “the moon” but with a reversed LP distribution (from  $-\pi/2$  to 0) and arc gradient (Fig. 3d, e).

According to the above design, we fabricated holographic LC superstructures I and II (see Additional file 1: Fig. S4 for their POM textures) and conducted the holographic experiment. When LC superstructure I is illuminated by RCP (LCP) light, the holographic image of “the moon” is reconstructed (Fig. 3f, g), which exhibits LCP (RCP) polarizations with continuously varied intensity distributions (denoted by the circles with arrows with different sizes) as expected. Through LP incidence, we reconstructed the intended holographic image, which encodes the customized vectorial information (Fig. 3h). With the help of an analyzer, the polarization information can be sorted. As we rotate the analyzer from  $-90^\circ$  to 0, the extinction region shifts from right to left in the

observed holographic pattern, which matches the different phases of the moon (Fig. 3i–l and Additional file 1: Fig. S5).

For LC superstructure II, the reconstructed holographic patterns under CP incidence (Fig. 3m, n) are the same as those from superstructure I but encoded with the orthogonal helicity. An inversed vectorial distribution is generated in the holographic image for LP incidence (Fig. 3o, spatially varied LP from  $-\pi/2$  to 0). Consequently, the extinction occurs from left to right when the polarization key changes from 0 to  $90^\circ$  (Fig. 3p–s). We note that the images in Fig. 3f–h, m–o correspond to the “full moon”, while the images in Fig. 3j, k, q, and r represent the phases of “last quarter half moon”, “waxing crescent moon”, “first quarter half moon”, and “waning crescent moon”, respectively. Remarkably, the vectorial holographic patterns generated from superstructures I and II during the polarization-sorting process constitute

the full phase diagram of the moon, and some typical lunar phase revolution images are provided in Additional file 1: Fig. S5.

## 2.4 Vectorial LC-holographic video

Leveraging the dynamic tunability of LC superstructures, we successfully achieved an active time-sequence vectorial holographic video (see the texture of holographic LC superstructure in Additional file 1: Fig. S6). Target video segment is selected from a famous football match “Man Utd 2-0 Portsmouth, 30 January 2008”, where a football player takes a free kick. As shown in Fig. 4a, we encode the regions of the football gate (purple) and competition score (blue) with LCP and RCP, respectively. The time-sequential frames of the player taking a free kick (green, yellow, red, and crimson) are encoded with different phase differences ( $\Delta\varphi_i$ ) between LCP and RCP, which

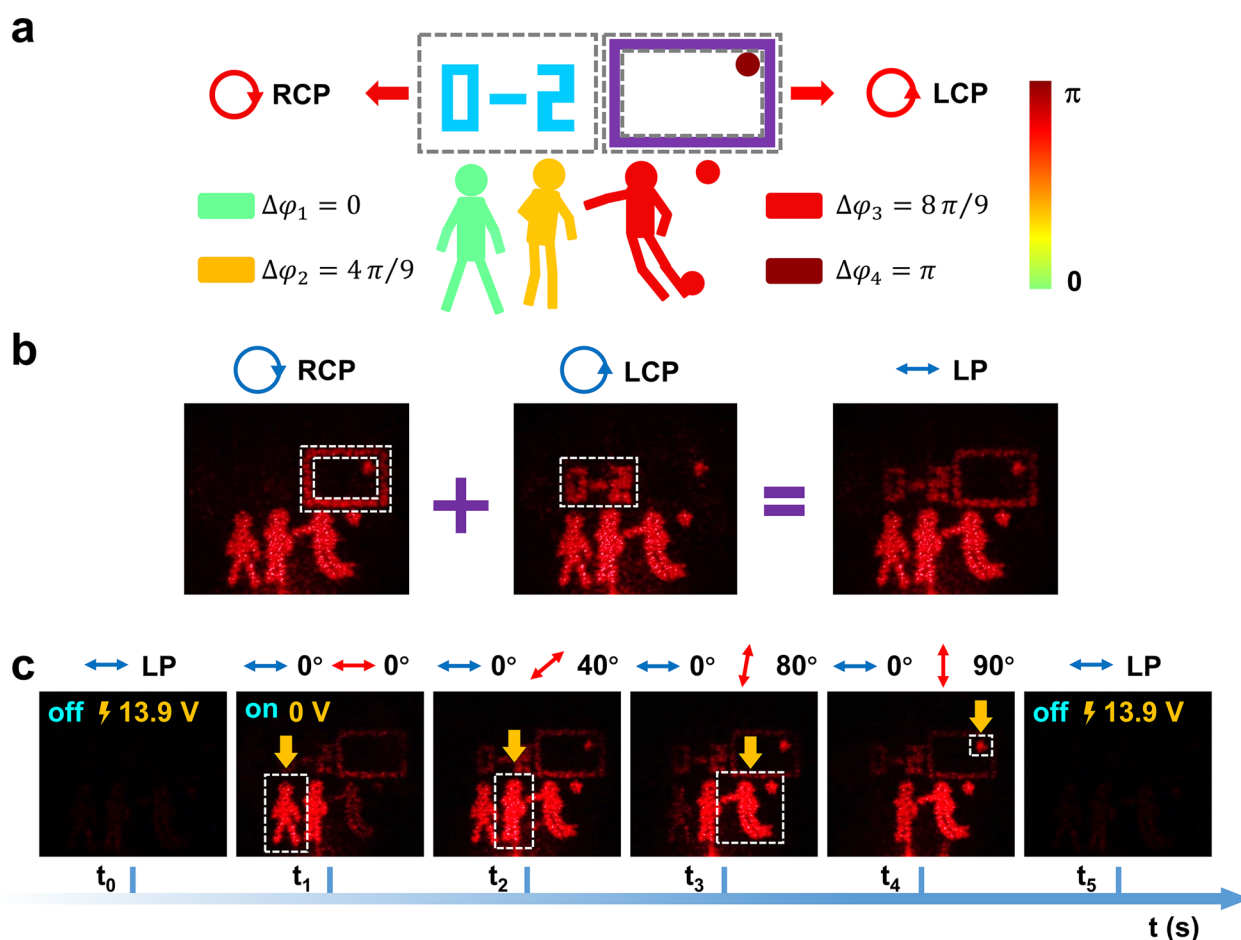


**Fig. 4** Electric-field and polarization addressable vectorial LC-holographic video. **a** Vectorial LC-holographic video design. The competition gate (score) is encoded with LCP (RCP). The images of time-dependent states of the foot player taking a free kick are embedded in the vectorial channels corresponding to the phase differences of  $\Delta\varphi_1=0, \Delta\varphi_2=4\pi/9, \Delta\varphi_3=8\pi/9,$  and  $\Delta\varphi_4=\pi$ . **b** Holographic images obtained at RCP, LCP, and LP incidence. **c** Electrically switchable and time-sequential polarization-addressable LC-holographic video display. The video is switched on/off at the applied voltage of 0 V/13.9 V (1 kHz square-wave signal)

allows us to create a multiplexed time sequence of holographic displays.

Figure 4b showcases the reconstruction of football gate, competition score, and the whole scenario of football match through RCP, LCP, and LP incidence, respectively, which is highly consistent with our design. With the aid of the electric field and the variation of polarization keys, the dynamic display of the holographic video with a high-quality and time-sequence performance has been experimentally demonstrated. At the beginning, the video is not played with the applied voltage of 13.9 V. In this stage, all channels for holographic images are closed due to the standing postures of LC directors, which lost the capability of optical waveform control. Once the electric field is removed, the LC molecules reorganize from standing postures to lying states. Thus, the holographic video is switched on (Fig. 4c). The holographic images corresponding to the positions of the player at different moments are selectively addressed in time sequence as the polarization key switches from 0° to 90°. Notably, both the gate (LCP) and score (RCP) consistently exist throughout the entire video segment to coincide with the real match scene. Each dynamic video frame presents the temporal state of the footballer with a high-quality holographic performance. After the player's free kick, the video display is electrically switched off. Due to the reconfigurable nature of LCs, this addressing process is reversible. By combining the electric field and polarization addressable dynamics in vectorial LC-holography, these results may facilitate more advanced smart devices for anticounterfeiting, optical manipulations, and so on.

### 3 Discussion

To summarize, we demonstrate the first prototype of vectorial LC-holography, which refers to the implementation of arbitrary vectorial holography using a single planar element comprised of a single-material LC, as opposed to using metamaterials combined with LCs or employing complex optical systems where one of the devices includes LC. Particularly, such vectorial LC-holography strategy can achieve full utilization of polarization channels, including CP, EP, and LP control (Additional file 1: Text S3 and Fig. S7), to boost the information-encoding capacity. By leveraging the sensitive responsiveness of LCs, we further demonstrate the electrically switching of time-sequence vectorial LC-holographic video and the dynamic vectorial holographic encryption (Additional

file 1: Fig. S8 and Additional file 2: Video S1). For the latter, we can only access encrypted information of “NJU LC” with the correct polarization key (Additional file 1: Text S4). The experimental results agree well with the design and demonstrate excellent broadband properties. With optimized voltages, we achieve relatively high holographic efficiencies up to 69.08%, 70.93%, and 63.23% for wavelength at 633 nm, 540 nm, and 470 nm, respectively. The merits of dynamic tunability, easy fabrication, high efficiency, broad bandwidth, cost-effectiveness, high-quality performance, large-area manufacturing, and versatility make LCs outperform most bulky optical components.

For vectorial LC-holography, the spatial resolution of the photopatterning system would be quite important. Hologram with higher spatial resolution would be less influenced by higher-order diffraction. It also correlates with an augmented capacity to reconstruct more details in the holographic image. In order to demonstrate the impact of spatial resolution on the vectorial holography, optical performances of three pixelated LC samples with different pixel sizes of  $a=1.1\ \mu\text{m}$ ,  $2.2\ \mu\text{m}$ , and  $4.4\ \mu\text{m}$  are examined (Additional file 1: Fig. S9). Evidently, the vectorial holographic quality degrades as the resolution decreases, and the current spatial resolution of  $1.1\ \mu\text{m}$  is good enough to fabricate desirable pixelated LCs for vectorial holography. It seems difficult to further elevate the resolution with current devices and methods due to the cell-type configuration and the axial ( $z$ ) resolution of the system. Fortunately, this limitation can be potentially surmounted by developing monolithic LC polymeric films.

Several possible future directions could broaden this work [43]. For example, with such high-resolution pixelated LC superstructures, we can rationally envision the potentially important developments of cutting-edge photonic technologies in the near future, such as LC-based diffractive neural networks [44] and topological photonic systems [45]. In addition, the three-dimensional cholesteric LC and blue phase LC systems would further inspire vectorial chiral-LC optics. By employing the emerging ferroelectric nematic LCs [46, 47], which naturally combine the local electric polarity and the orientation order of LCs (promising the second-order nonlinear optical response), we can anticipate more advancements in vectorial LC optics within the framework of nonlinear optics [48]. Moreover, through combining our recipe with geometric metasurfaces, the capacity is greatly elevated because now our LC is super-pixelated, and nearly infinite possibilities of local polarization and amplitude

combination could be engineered. This work addresses challenging issues associated with vectorial LC optics, which paves a wide and flat avenue to real-world impacts for advanced optical cryptography, super-resolution imaging, optical communications, information storage systems, and many other vectorial optical applications.

## 4 Methods

### 4.1 Materials

The photoalignment agent SD1 (DaiNippon Ink and Chemicals, Japan) was used for photopatterning. SD1 molecules are sensitive to the polarization of incident light. After absorbing ultraviolet photons, the dye molecules isomerize and finally tend to orientate perpendicularly to the local polarization because of their dichroic absorptions [49–51]. SD1 is rewritable and only the last photo-reorientation will be recorded, which drastically facilitates the photo-patterning process. After the LC is infiltrated, SD1 will locally guide the LC directors through intermolecular interactions. To validate the versatility of pixelated LC architectures, an available commercial nematic LC E7 (Jiangsu Hecheng Display Technology Co., Ltd., China) was adopted.

### 4.2 Fabrications

Indium-Tin-Oxide (ITO) coated glass substrates were first ultrasonically cleaned, then UV ozone cleaned. The alignment agent SD1 was dissolved in dimethylformamide at a concentration of 0.35 wt%, spin-coated onto the substrate, and annealed at 100 °C for 10 min. Two pieces of glass substrates were separated by 9 μm spacers and sealed with epoxy glue to form a cell. Then the empty LC cell is placed at the image plane of the digital micromirror device-based microlithography system to record the patterns of LC director distribution via a multistep partly overlapping exposure process with a synchronous polarization control. The nematic LC E7 was capillary filled into the photopatterned cell at 70 °C and slowly cooled to the room temperature, ultimately forming a pixelated LC superstructure. The photoalignment process is more efficient when the temperature is at 25 °C and the humidity is < 40%.

### 4.3 Characterizations

All experiments were performed at room temperature and in an ambient environment. The POM textures of pixelated LCs were obtained by a crossed polarizing optical microscope (DM2700P, Leica). The LC samples were illuminated by a 633 nm laser (TEM-F-633, Changchun

New Industries Optoelectronics Technology Co., Ltd., China). A supercontinuum laser (SuperK EVO, NKT Photonics, Denmark) combined with a multichannel acousto-optic tunable filter (SuperK SELECT, NKT Photonics, Denmark) was adopted as the laser source to demonstrate the broadband properties of vectorial LC-holography. We used a polarizer combined with a quarter wave plate (JCOPTIX, China) to sort different circularly polarized light. All the holographic images were captured by a commercial camera (EOS 850D, Canon, Japan). The AC electric signals were output by a function generator (33522B, Agilent Technologies Inc., USA) and amplified by a voltage amplifier (2340, TEGAM, USA). The Stokes parameters of the holographic image were measured by a Polarization Analyzer (SK010PA, Schäfer + Kirchhoff).

## Supplementary Information

The online version contains supplementary material available at <https://doi.org/10.1186/s43593-024-00061-x>.

**Additional file 1: Text S1.** Two-loop-iteration Gerchberg–Saxton algorithm for vectorial LC-holography. **Text S2.** Advanced photopatterning technique for high-resolution pixelated LC superstructure. **Text S3.** Vectorial LC-holography with full polarization (CP, EP, and LP) control. **Text S4.** Dynamically tunable and broadband vectorial LC-holographic encryption. **Figure S1.** Flow chart of the modified Gerchberg–Saxton algorithm for vectorial LC-holography. **Figure S2.** Designed phase profile of LC director distribution for vectorial holographic clock. **Figure S3.** Experimental setup for vectorial holography. **Figure S4.** POM textures of the holographic LC superstructures I and II for “the phase of the moon”. **Figure S5.** Vectorial holographic phase diagram of the moon. **Figure S6.** POM texture of holographic LC superstructure for vectorial holographic video. **Figure S7.** Vectorial LC-holographic images with arbitrary polarization states. **Figure S8.** Dynamic, broadband, and multichannel vectorial LC-holographic encryption. **Figure S9.** Impact of spatial resolution on vectorial holographic performance.

**Additional file 2: Video S1.** Vectorial holographic movie presenting reconstructed holographic images when rotating the analyzer from 45° to 135°.

## Acknowledgements

The authors gratefully appreciate Dr. Li-Chao Zhang and Dr. Han Cao from JCOPTIX China for their assistance in providing the Polarization Analyzer for this study.

## Author contributions

YL, CQ, LM, and ZW conceived the design of this work. ZW and LM developed the vectorial holographic optimization algorithm. ZW fabricated the vectorial LC samples. ZW and HZ performed the optical characterizations; YL, LM, and CQ directed and supervised the research. LM, ZW, CQ, ZZ, and YL contributed to the data analysis and discussion. LM, ZW, ZZ, and YL prepared the manuscripts; LM, ZW, CQ, ZZ, and YL revised the manuscripts; ZW, ZZ, HZ, YW, HY, WH, WC, HD, LM, CQ, and YL discussed the results and commented on the manuscript.

## Funding

The work was supported by the National Key Research and Development Program of China (Nos. 2022YFA1405000 and 2021YFA1202000); National Natural Science Foundation of China (No. 62375119); Natural Science Foundation of Jiangsu Province (No. BK20212004); Basic Research Program of Jiangsu Province (BK20232040); Fundamental Research Funds for the Central Universities (021314380231); L.L. Ma gratefully acknowledges the support of Young Elite Scientists Sponsorship Program by CAST (2022QNRC001), Xiaomi Young

Scholar Program, and Integrated Research Platform for Key Technologies (SAAT), Nanjing University.

#### Availability of data and materials

All data needed to evaluate the conclusions in the paper are present in the paper and supporting information. Additional data related to this paper may be requested from the authors.

#### Declarations

#### Ethics approval and consent to participate

Not applicable.

#### Consent for publication

Not applicable.

#### Competing interests

Cheng-Wei Qiu is an Editor for the journal, no other author has reported any competing interests.

Received: 17 October 2023 Revised: 29 January 2024 Accepted: 12 February 2024

Published online: 05 March 2024

#### References

1. D.E. Smalley, Q.Y.J. Smithwick, V.M. Bove, J. Barabas, S. Jolly, Anisotropic leaky-mode modulator for holographic video displays. *Nature* **498**(7454), 313–317 (2013)
2. H. Ren, X. Fang, J. Jang, J. Burger, J. Rho, S.A. Maier, Complex-amplitude metasurface-based orbital angular momentum holography in momentum space. *Nat. Nanotechnol.* **15**(11), 948–955 (2020)
3. J. Li, S. Kamin, G. Zheng, F. Neubrech, S. Zhang, N. Liu, Addressable metasurfaces for dynamic holography and optical information encryption. *Sci. Adv.* **4**(6), eaar6768 (2018)
4. A.H. Dorrah, F. Capasso, Tunable structured light with flat optics. *Science* **376**(6591), eabi6860 (2022)
5. J. Hou, G. Situ, Image encryption using spatial nonlinear optics. *eLight* **2**(1), 3 (2022)
6. Y. Ding, Q. Yang, Y. Li, Z. Yang, Z. Wang, H. Liang et al., Waveguide-based augmented reality displays: perspectives and challenges. *eLight* **3**(1), 24 (2023)
7. G. Makey, Ö. Yavuz, D.K. Kesim, A. Turnali, P. Elahi, S. Ilday et al., Breaking crosstalk limits to dynamic holography using orthogonality of high-dimensional random vectors. *Nat. Photonics* **13**(4), 251–256 (2019)
8. L. Jin, Y.W. Huang, Z. Jin, R.C. Devlin, Z. Dong, S. Mei et al., Dielectric multi-momentum meta-transformer in the visible. *Nat. Commun.* **10**(1), 4789 (2019)
9. X. Fang, H. Ren, M. Gu, Orbital angular momentum holography for high-security encryption. *Nat. Photonics* **14**(2), 102–108 (2019)
10. H. Gao, X. Fan, W. Xiong, M. Hong, Recent advances in optical dynamic meta-holography. *Opto-Electron. Adv.* **4**(11), 210030–210030 (2021)
11. Y. Gao, L. Cao, Iterative projection meets sparsity regularization: towards practical single-shot quantitative phase imaging with in-line holography. *Light Adv. Manuf.* **4**(1), 37–53 (2023)
12. B. Xiong, Y. Liu, Y. Xu, L. Deng, C.W. Chen, J.N. Wang et al., Breaking the limitation of polarization multiplexing in optical metasurfaces with engineered noise. *Science* **379**(6629), 294–299 (2023)
13. N.A. Rubin, A. Zaidi, A.H. Dorrah, Z. Shi, F. Capasso, Jones matrix holography with metasurfaces. *Sci. Adv.* **7**(33), eabg7488 (2021)
14. W. Han, Y. Yang, W. Cheng, Q. Zhan, Vectorial optical field generator for the creation of arbitrarily complex fields. *Opt. Express* **21**(18), 20692–20706 (2013)
15. N.S. Bisht, V. Tiwari, *Spatial Light Modulators and Their Applications in Polarization Holography* (IntechOpen, London, 2022)
16. Q. Song, A. Baroni, R. Sawant, P. Ni, V. Brandli, S. Chenot et al., Ptychography retrieval of fully polarized holograms from geometric-phase metasurfaces. *Nat. Commun.* **11**(1), 2651 (2020)
17. N.V. Petrov, B. Sokolenko, M.S. Kulya, A. Gorodetsky, A. Chernykh, V. Design of broadband terahertz vector and vortex beams: I. review of materials and components. *Light Adv. Manuf.* **3**(4), 640–652 (2022)
18. X. Li, L. Chen, Y. Li, X. Zhang, M. Pu, Z. Zhao et al., Multicolor 3D meta-holography by broadband plasmonic modulation. *Sci. Adv.* **2**(11), e1601102 (2016)
19. Q. Ma, W. Gao, Q. Xiao, L. Ding, T. Gao, Y. Zhou et al., Directly wireless communication of human minds via non-invasive brain-computer-metasurface platform. *eLight* **2**(1), 11 (2022)
20. H. Gao, Y. Wang, X. Fan, B. Jiao, T. Li, C. Shang et al., Dynamic 3D meta-holography in visible range with large frame number and high frame rate. *Sci. Adv.* **6**(28), eaba8595 (2020)
21. G. Qu, W. Yang, Q. Song, Y. Liu, C.W. Qiu, J. Han et al., Reprogrammable meta-hologram for optical encryption. *Nat. Commun.* **11**(1), 5484 (2020)
22. H. Yang, K. Ou, H. Wan, Y. Hu, Z. Wei, H. Jia et al., Metasurface-empowered optical cryptography. *Mater. Today* **47**, 424 (2023)
23. J.P. Balthasar Mueller, N.A. Rubin, R.C. Devlin, B. Groever, F. Capasso, Metasurface polarization optics: independent phase control of arbitrary orthogonal states of polarization. *Phys. Rev. Lett.* **118**(11), 113901 (2017)
24. X. Zhang, S. Yang, W. Yue, Q. Xu, C. Tian, X. Zhang et al., Direct polarization measurement using a multiplexed Pancharatnam-Berry metahologram. *Optica* **6**(9), 1190–1198 (2019)
25. D. Wen, J.J. Cadusch, J. Meng, K.B. Crozier, Vectorial holograms with spatially continuous polarization distributions. *Nano Lett.* **21**(4), 1735–1741 (2021)
26. R. Zhao, B. Sain, Q. Wei, C. Tang, X. Li, T. Weiss et al., Multichannel vectorial holographic display and encryption. *Light Sci. Appl.* **7**, 95 (2018)
27. L.L. Ma, C. Liu, S.B. Wu, P. Chen, Q.M. Chen, J.X. Qian et al., Programmable self-propelling actuators enabled by a dynamic helical medium. *Sci. Adv.* **7**(32), eabh3505 (2021)
28. H.K. Bisoyi, Q. Li, Light-driven liquid crystalline materials: from photo-induced phase transitions and property modulations to applications. *Chem. Rev.* **116**(24), 15089–15166 (2016)
29. L.L. Ma, S.B. Wu, W. Hu, C. Liu, P. Chen, H. Qian et al., Self-assembled asymmetric microlenses for four-dimensional visual imaging. *ACS Nano* **13**(12), 13709–13715 (2019)
30. Z. Zheng, H. Hu, Z. Zhang, B. Liu, M. Li, D.-H. Qu et al., Digital photoprogramming of liquid-crystal superstructures featuring intrinsic chiral photoswitches. *Nat. Photonics* **16**(3), 226–234 (2022)
31. Y. Ni, C. Chen, S. Wen, X. Xue, L. Sun, Y. Yang, Computational spectropolarimetry with a tunable liquid crystal metasurface. *eLight* **2**(1), 23 (2022)
32. J. Kim, Y. Li, M.N. Miskiewicz, C. Oh, M.W. Kudenov, M.J. Escuti, Fabrication of ideal geometric-phase holograms with arbitrary wavefronts. *Optica* **2**(11), 958–964 (2015)
33. L.L. Ma, C.Y. Li, J.T. Pan, Y.E. Ji, C. Jiang, R. Zheng et al., Self-assembled liquid crystal architectures for soft matter photonics. *Light Sci. Appl.* **11**(1), 270 (2022)
34. J. Kobashi, H. Yoshida, M. Ozaki, Planar optics with patterned chiral liquid crystals. *Nat. Photonics* **10**(6), 389–392 (2016)
35. D. Tang, Z. Shao, Y. Zhou, Y. Lei, L. Chen, J. Xie et al., Simultaneous surface display and holography enabled by flat liquid crystal elements. *Laser Photonics Rev.* **16**(7), 2100491 (2022)
36. P. Chen, Z.X. Shen, C.T. Xu, Y.H. Zhang, S.J. Ge, L.L. Ma et al., Simultaneous realization of dynamic and hybrid multiplexed holography via light-activated chiral superstructures. *Laser Photonics Rev.* **16**(5), 2200011 (2022)
37. Z. Wang, H. Zhang, X. Liu, Y. Dou, D. Wei, W. Chen et al., Cascaded liquid crystal holography for optical encryption. *Chin. Opt. Lett.* **12**, 120003 (2023)
38. J. Li, P. Yu, S. Zhang, N. Liu, Electrically-controlled digital metasurface device for light projection displays. *Nat. Commun.* **11**(1), 3574 (2020)
39. I. Kim, J. Jang, G. Kim, J. Lee, T. Badloe, J. Mun et al., Pixelated bifunctional metasurface-driven dynamic vectorial holographic color prints for photonic security platform. *Nat. Commun.* **12**(1), 3614 (2021)
40. M. Abu Aisheh, M. Abutoama, M.J. Abuleil, I. Abdulhalim, Fast tunable metamaterial liquid crystal achromatic waveplate. *Nanophotonics* **12**(6), 1115–1127 (2023)
41. Y. Hu, X. Ou, T. Zeng, J. Lai, J. Zhang, X. Li et al., Electrically tunable multifunctional polarization-dependent metasurfaces integrated with liquid crystals in the visible region. *Nano Lett.* **21**(11), 4554–4562 (2021)

42. Z.E. Bomzon, G. Biener, V. Kleiner, E. Hasman, Space-variant Pancharatnam–Berry phase optical elements with computer-generated subwavelength gratings. *Opt. Lett.* **27**, 1141–1143 (2002)
43. C. Wan, A. Chong, Q. Zhan, Optical spatiotemporal vortices. *eLight* **3**, 11 (2023)
44. X. Lin, Y. Rivenson, N.T. Yardimci, M. Veli, Y. Luo, M. Jarrahi et al., All-optical machine learning using diffractive deep neural networks. *Science* **361**(6406), 1004–1008 (2018)
45. H. Abbaszadeh, M. Fruchart, W. van Saarloos, V. Vitelli, Liquid-crystal-based topological photonics. *Proc. Natl. Acad. Sci. U.S.A.* **118**(4), e2020525118 (2021)
46. X. Chen, E. Korblova, D. Dong, X. Wei, R. Shao, L. Radzihovsky et al., First-principles experimental demonstration of ferroelectricity in a thermotropic nematic liquid crystal: polar domains and striking electro-optics. *Proc. Natl. Acad. Sci. U.S.A.* **117**(25), 14021–14031 (2020)
47. O.D. Lavrentovich, Ferroelectric nematic liquid crystal, a century in waiting. *Proc. Natl. Acad. Sci. U.S.A.* **117**(26), 14629–14631 (2020)
48. N. Mao, G. Zhang, Y. Tang, Y. Li, Z. Hu, X. Zhang et al., Nonlinear vectorial holography with quad-atom metasurfaces. *Proc. Natl. Acad. Sci. U.S.A.* **119**(22), e2204418119 (2022)
49. W. Zhang, A. Srivastava, V. Chigrinov, H. S. Kwok. Optically rewritable liquid crystal display. (*E-Paper Displays*, 2022), pp. 171–196
50. V. Chigrinov, S. Pikin, A. Verevochnikov, V. Kozenkov, M. Khazimullin, J. Ho et al., Diffusion model of photoaligning in azo-dye layers. *Phys. Rev. E* **69**(6), 061713 (2004)
51. L.-L. Ma, S.-S. Li, W.-S. Li, W. Ji, B. Luo, Z.-G. Zheng et al., Rationally designed dynamic superstructures enabled by photoaligning cholesteric liquid crystals. *Adv. Opt. Mater.* **3**, 1691–1696 (2015)